Journal of Physics D: Applied Physics

PAPER

Emulating artificial neuron and synaptic properties with SiO_2-based memristive devices by tuning threshold and bipolar switching effects

To cite this article: Panagiotis Bousoulas *et al* 2021 *J. Phys. D: Appl. Phys.* **54** 225303

IOP Publishing Journal of Physics D: Applied Physics

J. Phys. D: Appl. Phys. **54** (2021) 225303 (9pp) https://doi.org/10.1088/1361-6463/abea3b

Emulating artificial neuron and synaptic properties with SiO_2-based memristive devices by tuning threshold and bipolar switching effects

Panagiotis Bousoulas[1,*], Marianthi Panagopoulou[1], Nikos Boukos[2] and Dimitris Tsoukalas[1]

[1] Department of Applied Physics, National Technical University of Athens, Iroon Polytechniou 9 Zografou, 15780 Athens, Greece
[2] Institute of Nanoscience and Nanotechnology, NCSR 'Demokritos', Aghia Paraskevi, 15310 Athens, Greece

E-mail: panbous@mail.ntua.gr

Received 2 January 2021, revised 14 February 2021
Accepted for publication 26 February 2021
Published 9 March 2021

Abstract

The implementation of neuromorphic computations within a fully memristive neural network is considered the holy grail of the artificial intelligence era. In order to attain this goal, it is quite important to develop robust and configurable electronic devices capable of emulating spiking neuronal and synaptic plasticity activities. Along these lines, we report here the direct impact of oxygen concentration as well as of the homo-bilayer material configuration of SiO_2-conductive bridge memories to the manifestation of tunable threshold and bipolar switching effects. Interestingly, while the bilayer structure of Ag/SiO_x/SiO_y/TiN ($x < y$) exhibits only bipolar switching effect, the respective single-layer structures of Ag/SiO_y/TiN and Ag/SiO_x/TiN operate under either threshold switching or both modes. Insights regarding the impact of oxygen concentration into the conducting filament growth process are provided. The manifestation of the two switching modes permits the emulation of various synaptic effects, such as short-term plasticity and long-term plasticity whereas the modulation of the conductance values allows the synaptic weight tuning by controlling the amplitude or the frequency of the triggering signals. Moreover, arbitrary neuron characteristics were obtained from our volatile memory devices without integrating any other auxiliary circuit. Our approach provides valuable insights towards the realization of artificial neural networks from the same material configuration with biological-like dynamic behavior.

Supplementary material for this article is available online

Keywords: oxygen concentration, conducting filament, neuron, memristor, threshold switching, synapse

(Some figures may appear in colour only in the online journal)

* Author to whom any correspondence should be addressed.

1. Introduction

Neuromorphic engineering is poised to revolutionize information technologies by developing—among others—electronic devices that emulate biological neural networks at the hardware level. The conventional state-of-the-art computational systems are experiencing tremendous difficulties when they are dealing with big amount of unstructured data and real-time decision-making processes. The underlying reason behind this incompetence is the von Neumann operating principle that dictates the constant transferring of data between the processing and store units, with a strictly sequential algorithm. On the other hand, a completely different picture takes place within the human brain, where a colossal parallel information procedure occurs. This striking contrast between these two computational models necessitates the need of devising new architectures that will permit the fabrication of novel intelligent computational platforms with inherent in-the-field learning capabilities [1]. Along these lines, the appearance of resistive switching devices with rich internal dynamic processes pave the way towards the implementation of novel hardware-based neural networks with low leakage power dissipation [2]. The key features of an artificial neural network are the synaptic and neuron elements. The role of the synapse is to control the flow of information by weight modulation whereas the neuron assembles the information and release it (fire activity) if a threshold value is met. Although there are several works in the literature regarding the utilization of the resistive switching effect towards the implementation of artificial synaptic and neuron characteristics [3–5], their integration into a fully memristive neural network it is not trivial, since the design requirements of artificial synapse are quite different with respect to artificial neuron. Moreover, the attempts to employ discrete resistive neuron and synapse electronic elements in order to build a fully memristive neural network increases dramatically both the design and fabrication complexity between these two platforms [6, 7]. To address these challenges, it is apparent that a physics-driven device engineering is required in order to implement fully integrated memristive neural network, by utilizing the same material configuration [8–10]. Conductive bridge memories (CBRAM) arise as a suitable candidate towards that direction, due to the inherit dynamics of the switching processes. More specific, the rich nature of the switching effect within CBRAM configuration permits the manifestation of various switching modes, such as threshold and bipolar switching, under the same memory element. This is of vital importance, since the spontaneous decay of the current values during the threshold switching is closely related with the spiking activity, whereas the modulation of the conducting filament's (CF's) resistance can lead to the desirable synaptic plasticity patterns.

Under this perspective, we present here a systematic study of the impact of oxygen concentration and material configuration into the manifestation pattern of the various switching modes. Since the diffusion of silver ions is strongly dependent from the presence of oxygen within the device active core, we can control the effective CF's diameter and attain reconfigurable resistive and neuromorphic properties [11].

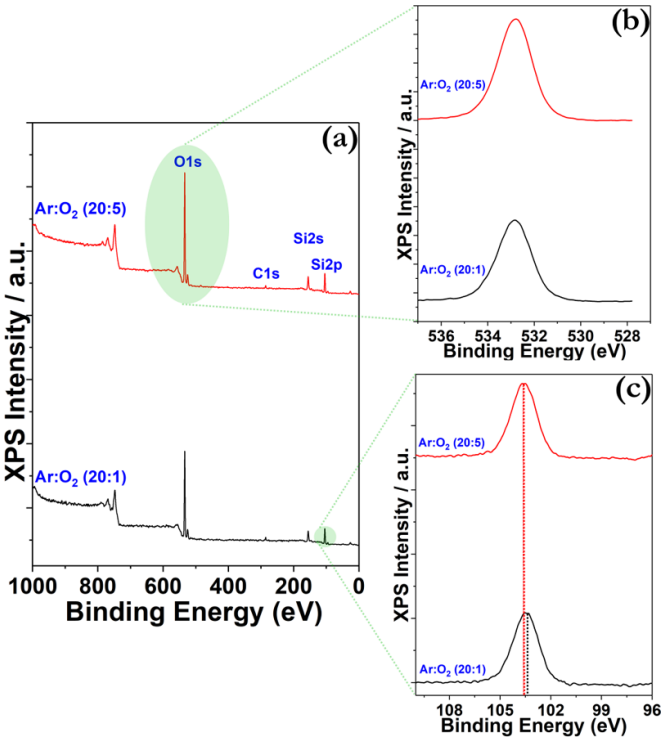

Figure 1. (a) XPS spectrum of two SiO_2 thin films grown on Si substrates, (b) O1s and (c) Si2p XPS peaks of the two samples, respectively.

For that reason, single-layer devices of Ag (∼40 nm)/SiO_y (∼20 nm)/TiN (40 nm) (sample A) and Ag (∼40 nm)/SiO_x (∼20 nm)/TiN (40 nm) (sample B) as well as bilayer structures of Ag (∼40 nm)/SiO_x (∼10 nm)/SiO_y (∼10 nm)/TiN (40 nm) (sample C) were fabricated and thoroughly examined. The thickness of each film was measured in test samples by performing both line scan with surface profiler and ellipsometry. The x-ray photo-electron spectroscopy (XPS) measurements corroborate the scenario that an elevated oxygen flux during the SiO_2 deposition leads to an increased oxygen content, indicating that a meticulous control over the growth mechanism of the active material is quite important for the emulation of various novel electrical properties.

2. XPS measurements

The growth mechanism of the SiO_2 films was confirmed by XPS measurements, as can be ascertained from the results presented in figure 1. The scans of the samples A and B revealed the presence of several peaks that correspond to Si, O and C atoms. In figure 1(b) the O1s is shown that consists of one component at binding energy 532.8 eV whereas in figure 1(c) the Si2p peak consists of one component at binding energy at 130.5 eV. Both peaks are assigned to SiO_2 according to the literature [12, 13]. The samples present a superficial carbon contamination from the atmosphere and the C1s is centered at 284.8 eV. A small part of the O1s peak area associated with the CO_x contribution in the C1s spectra is subtracted from the oxygen peak area. All experiments were carried out

within a high vacuum chamber ($\sim 10^{-10}$ mbar) so the impact of oxygen is negligible.

Moreover, the detailed spectrum of Ar2p revealed the presence of small amount of Ar, showed in figure S1 (available online at stacks.iop.org/JPD/54/225303/mmedia) (supporting information). The relative atomic ratio of Si and O atoms is estimated from the peak areas of the Si2p and O1s XPS peaks divided by the relative sensitivity factors (RSFs) and the electron analyzer transmission function. The surface atomic ratios of the Si and O were calculated from the intensity (area) of the XPS peaks weighted with the corresponding RSF ratios and the electron energy analyzer transmission characteristics. The RSF derived from the Scofield cross sections, σ, adjusted for angular asymmetry for photoemission, the electron transport properties of the matrix, namely the inelastic mean free path λi and the density. The results divulged that the stoichiometry degree of sample A is $SiO_{2.07}$ and of sample B is SiO_2. Similar results have been reported in the literature for room temperature-based depositions of SiO_2 thin films by the magnetron sputtering technique and by employing comparable oxygen flows with these used in this work [14, 15].

It is also interesting to remark that from the Si2p spectrum (figure 1(c)) a slight but discernible shift of the respective peak towards higher binding energies is observed. Similar effects have been reported by other works [16, 17], suggesting that as the oxygen content increases during the film growth a charge transfer effect takes place from O to Si atoms when the Si–O bonds are formed. This result indicates that the oxygen growth rate not only determines the stoichiometry of the various oxide films but also determines the energy favorable tetrahedral configuration of the oxygen atoms around the central Si atom [18]. The shape of these configurations is quite critical for the diffusion of ionic species through these materials. Moreover, the oxygen content has a direct impact on the distribution of the various electronic states of the SiO_2. While the conduction band is not practically affected while the oxygen content is increasing, within the valence band that consists of Si–Si states, Si–O bonding states start to appear. This leads to the strong localization of the Si–Si bonding states and the subsequent reduction of the density of defects, since the potential existence of weak Si–Si bonds are replaced by the abundant neighboring oxygen atoms [19].

3. Electrical performance evaluation

3.1. *I–V characteristics*

Figure 2 depicts the direct current (DC) *I–V* characteristics obtained by the application of external bias to the top electrode (TE), while keeping the bottom electrode (BE) grounded. A compliance current (I_{cc}) limit was enforced only for sample B during the manifestation of the bipolar switching mode, whereas in the rest cases a self-compliance behavior was observed. Moreover, no electroforming process was required prior device operation. Three distinct patterns are captured for the three different samples: sample A exhibits bidirectional threshold switching (figure 2(a)), sample B operates at both one-directional threshold (figure 2(b)) and bipolar

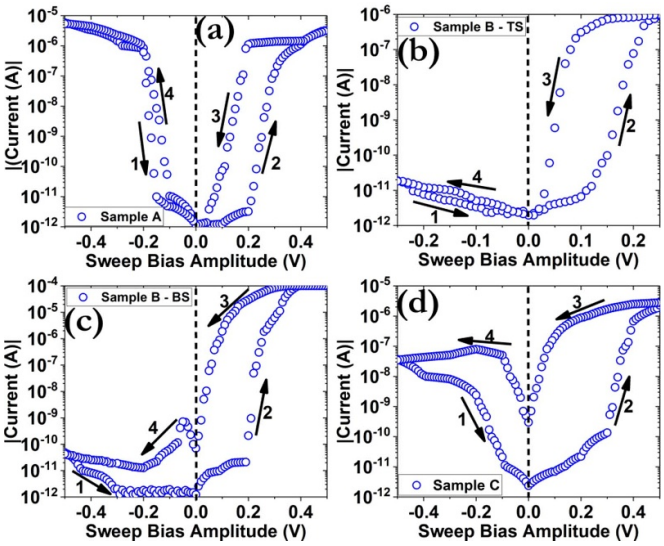

Figure 2. *I–V* hysteresis curves for all samples considered in this work. A cycling bias of 0.5 V was applied for (a) sample A, (c) sample B—BS (bipolar switching) and (d) sample C—TS (threshold switching) whereas for sample B a smaller cycling bias of (b) 0.25 V was enforced in order to observe the threshold switching effect. The arrows in the graphs signify the switching direction while the sweep rate was 10 mV s^{-1}. Similar switching patterns were captured by starting the sweeps from 0 V to $|V_{max}|$ (not shown here). The underlying idea to start sweeps from negative voltage is to automate the consecutive cycling measurement procedure. The finite current values of the samples that exhibit the bipolar switching mode in the absence of an external stimulus (switching direction 3) are associated with the incomplete rupture of the CF. In any case, the measured current values are quite small.

switching mode (figure 2(c)—depending on the amplitude of the external bias) whereas sample C displays only the bipolar switching mode (figure 2(d)). These memory patterns are maintained under 100 consecutive device cycling operation, without any significant degradation (figure S2—supporting information). The switching ratio for the Samples that operate at the threshold switching mode is about $\sim 10^4$ while an even higher memory window is recorded for the bipolar switching mode ($\sim 10^5$—figure S3—supporting information).

There are also some key differences between the three samples that signify a quite different CF growth mode. The self-rectification ratios are larger for the sample B, while samples A and C present no or very small rectification properties (figure S4—supporting information). Moreover, the V_{SET} takes place at about $\sim$0.2 V for samples A and B, whereas the set transition for sample C is recorded at $\sim$0.3 V. Furthermore, sample C divulges the smaller operating current values for the low-resistance-state (LRS) as well as the smaller slopes during set transition (figure S5—supporting information). The high-resistance-state (HRS) does not seem to be affected from the different oxygen contents.

3.2. *Artificial neuron activity*

The spontaneous relaxation to the HRS through the threshold switching effect can be leveraged in order to achieve artificial

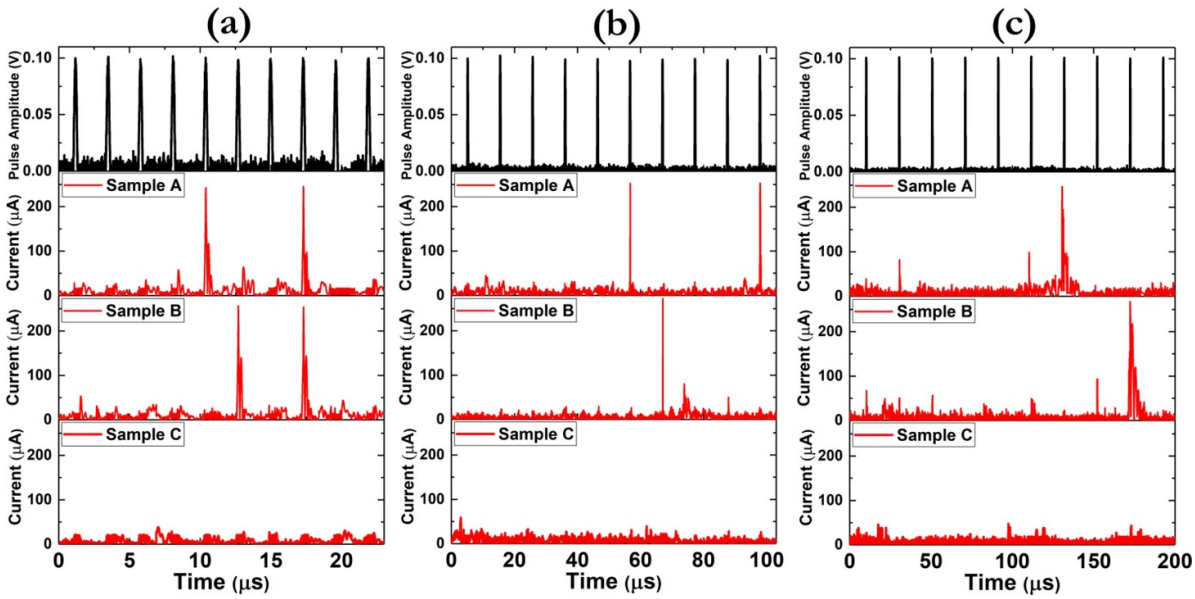

Figure 3. Transient response of all samples under the execution of spiking neuron protocol with the application of pulses of (a) 1 MHz, (b) 500 kHz and (c) 100 kHz frequency, respectively. A pulse width of 100 ns and amplitude of 100 mV was enforced in all cases.

neuron properties. Within the brain configuration, the neurons encrypt information packages by emitting small voltage pulses that are called action potentials or spiking neuronal signals. An artificial neuron should comprise the functionalities of automatic firing activity, leaky integration and sharp recovery [20]. The interpretation of above-mentioned spontaneous decay process of the CF is still under debate, albeit the surface energy minimization [21] and the out diffusion of metal ions due to intense local Joule heating [11] are considered the driving forces behind this behavior. In any case, the existence of an intrinsic threshold switching effect reduces significantly the supporting electrical circuit that is required in order to realize the leaky integrate and fire functionalities of a neuron [22], without the necessity for including external comparators [23]. In the majority of artificial neuron circuits the threshold switching device is connected in parallel with a leaky capacitor [24] while an intense effort is currently underway in order to get rid of this external capacitor, by attaining leaky-type behavior in conjunction with threshold switching [25, 26]. In order to examine whether our devices can emulate an artificial neuronal activity, we subjected them into an array of pulse tests. Initially, a train of 10 pulses with amplitude 100 mV or 200 mV, width of 100 ns and frequency of 10 MHz was enforced to all devices. The results (figure S6—supporting information) divulged no response for sample C, whereas for the other two samples a continuous post-synaptic feedback was acquired, similar to the paired-pulse-facilitation (PPF) patterns. This outcome is anticipated by taking into account that our prototypes exhibit quite short relaxation times ($\sim$100 ns) [11] and thus there is no available time between the consecutive pulses in order to allow the full recovery of our devices [27]. Subsequently, we have applied a train of identical pulses with longer delay times (1 μs, 5 μs and 10 μs) and same amplitude and width as previously. The results that are presented in figures 3 and S7 (supporting information), display indeed the existence of various arbitrary current peaks for samples A and B, in direct contrast with sample C, where no peaks are apparent.

It is interesting to notice that after each spiking event the peaks are disappeared which is attributed to the quick dissolution of sub-nm scale CF. One other remarkable feature of our devices is the assumption that due to electrodes' materials thermal conductivity distribution, the CF is anticipated to be disrupted near the BE [11]. As a result, the largest part of the CF is expected to remain intact (leaky capacitor) and the implementation of artificial spiking neuronal activities will take place with a tunable manner at various frequencies. However, the subsequent CF growth can take place through dendritic processes that are random by nature. As a result, the subsequent spiking activity can be considered rather random and no reproducible pattern was observed from the analysis of our data. This issue can be addressed by incorporating novel 2D materials within the switching matrix in order to more precisely control the ionic flux [28] or employing sophisticated external circuits [29].

Besides the above issue, we were still able to detect a pattern regarding the number of pre-synaptic pulses that are required in order to record the first spiking activity. The results that are presented in figure 4 indicate that sample A always exhibit artificial neuron properties under the application of a smaller number of pre-synaptic pulses and the latter number is decreasing when we either increase the pulse amplitude or the frequency of the pulse train. This effect is believed to be associated with the steep transition slopes of sample A that are $\sim$35% larger with respect to sample B, signifying that with proper control over the defect density of the switching material we can attain several interesting neuromorphic features [30].

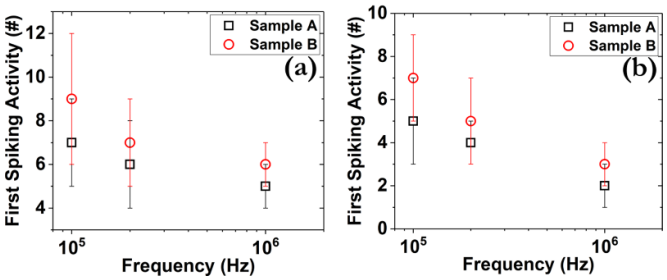

Figure 4. Distribution of the number of pre-synaptic spikes required in order to record a post-synaptic neuron activity as a function of the frequency, during the application of (a) 100 mV and (b) 200 mV pulse amplitude. The data have been collected from 20 different memory cells from each sample.

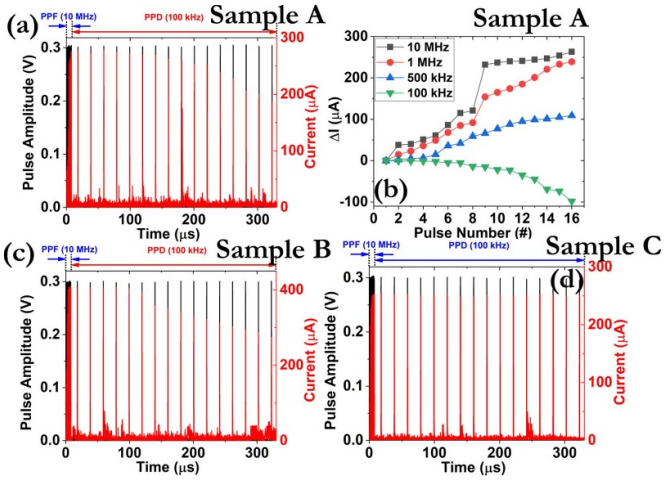

Figure 5. Artificial synaptic characteristics of all samples by monitoring the current response under the application of a train of 32 consecutive pulses with same width (100 ns) and different frequency. Samples (a) A and (c) B are experiencing short-term synaptic PPF to PPD transition when the frequency of the stimulation decreases from 10 MHz to 100 kHz, whereas (d) sample C retains its current values for the whole measurement time scale. The duration between the pulses determines the synaptic weight pattern, as can be asserted from (b), where the change in measured current is depicted (the respective data have been collected from sample A).

It is also interesting to notice that we can relate the different spiking neuron responses acquired at different frequencies by calculating the different RC delay constants of the respective capacitors. For that reason, we performed capacitance–voltage (C–V) measurements in order to extract the values of capacitance that correspond to the LRS (figure S8—supporting information—read-out voltage 0.5 V) [31], while the resistance values were extracted by applying single pulses with amplitude of either 100 or 200 mV and width 100 ns (not shown here). The theoretical results are in line with the experimental ones, since for instance for sample A the first spiking activity after the application of a train of pre-synaptic signals of 1 MHz frequency and 100 mV amplitude (figure 3(a)) takes place at about 10 μs which is comparable with the delay time of the respective capacitor ($\tau = R \times C = 10^7$ Ohm $\times$ 1.1 $\times$ 10^{-12} F $= 11$ μs). Similar calculations can be found at table S1, indicating that acquiring direct control over the time delay distribution of the respective capacitor-like structures is quite crucial for attaining reconfigurable synaptic properties [32].

3.3. *Artificial synapse activity*

Along with the distribution of neurons in the brain, the vast grid of synapses creates a biological neural network that is responsible for the human emotion, perception, forgetting, learning and memory tasks [33]. While neurons operate towards the generation and propagation of action potential, the synapses are responsible for the processing and storage procedures. Here we focus on a variety of synaptic property characteristics, such as PPF, paired-pulse depression (PPD) which belong to the category of short-term plasticity (STP) effects as well as to long-term plasticity (LTP) effects. The former are responsible for the training of the synapse while the later are correlated with the permanent memory capabilities. During PPF/PPD procedures the second post-synaptic signal becomes larger/smaller in contrast with the first response, when a set of two identical consecutive stimuli are enforced. All the above properties are nicely captured by our devices, as it is depicted in figure 5. A high/low frequency leads to an increase/decrease of the current response from the initial state and as a result to clear demonstration of bio-synaptic properties (figure S9—supporting information) [34]. This scenario does not apply for sample C, which retains its current values even when the frequency of the pulses is reduced from 10 MHz to 100 kHz, and negative pulses are required in order to observe the synaptic depression effect (figure S10—supporting information).

Moreover, in direct comparison with biological synapses, we have examined the memory loss properties. According to the well-established model of Atkinson and Shiffrin the memory consists of three different constituents: the sensory, short-term and long-term memories (figure S11—supporting information) [35]. Depending on the properties of the input signals (i.e. frequency, amplitude) a transition from short-term to long-term memory can be induced. In the same way, we can impose STP to LTP conversion in our artificial synaptic elements by applying a train of consecutive pulses. The results presented in figure 5 reveal different patterns for the synaptic weight distribution.

When the triggering pulses are removed, the current profile starts to decay quite fast for all samples. However, it is interesting to notice that for samples B and C (figures 6(b) and (c)), the synaptic weights are not diminished to their initial OFF-state but remain to an intermediate state which is equivalent to the LTP transition. In contrast sample A relaxes quite shortly to the initial state that corresponds to the STP procedure (figure 6(a)).

The synaptic weight distribution is presented in figure 6(d) where the memory decay pattern is captured with the following expression:

$$y = b \times t^{-m} \tag{1}$$

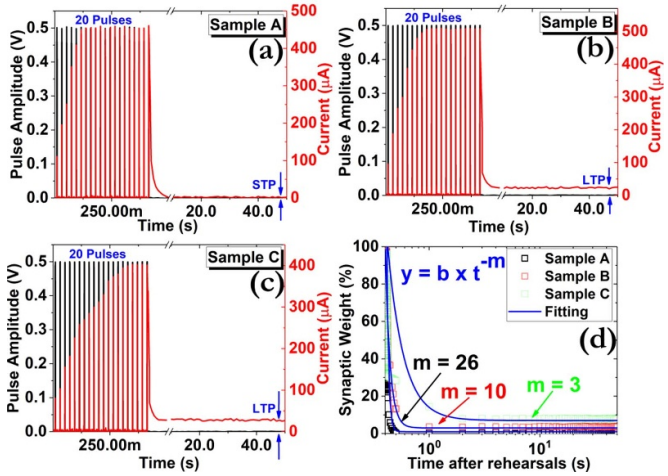

Figure 6. Experimental demonstration of STP and LTP characteristics under the application of a train of 20 pulses with 0.5 V amplitude, 1 ms width and delay 10 ms. While (b) sample B and (c) sample C retain their current values even for 50 s, (a) sample A quickly returns to the HRS. (d) The synaptic weight distribution is smoothly modeled by the exponential decay fitting curve. It is also interesting to notice the good linearity current response of sample C in contrast with the other two samples that their current values saturate after the application of about 5 and 8 pre-synaptic pulses.

where b is a scaling constant, t is the time and m is a constant related to the relaxation time [36]. The smaller the m the higher the memory durability, as can be confirmed from the fitting results. A sharp decay within 10 ms after the rehearsals take place for sample A whereas a saturation level is maintained for samples B and C for 50 s [37]. These responses are consistent with the respective volatile states of each sample, since the LTP state is strongly correlated with the retention capability of each sample. Interestingly, by reducing the pulse height to 0.3 V, only sample C divulges LTP related characteristics (figure S9—supporting information).

4. Discussion

From the above analysis it is apparent that the oxygen content within the active switching material plays a key role towards the emulation of various neuromorphic properties on demand, since they can practically control the CF growth/dissolution mechanism. The filamentary scenario stems primarily from the insensitivity of the LRS from the total device area (figure S13(a)—supporting information) whereas the temperature dependence of the respective resistance values indicates the metallic nature of the constituents of the CF (figure S13(b)—supporting information). The whole memristive performance can be nicely interpreted by taking into account the impact of the thermo-diffusion mechanism on the spatial evaluation of the effective CF's diameter [11]. Moreover, a recent study in SiO_2-based memristors revealed that defect density smaller that 10^{-3} parts-per-million can dramatically affect the whole memory performance [30]. Here

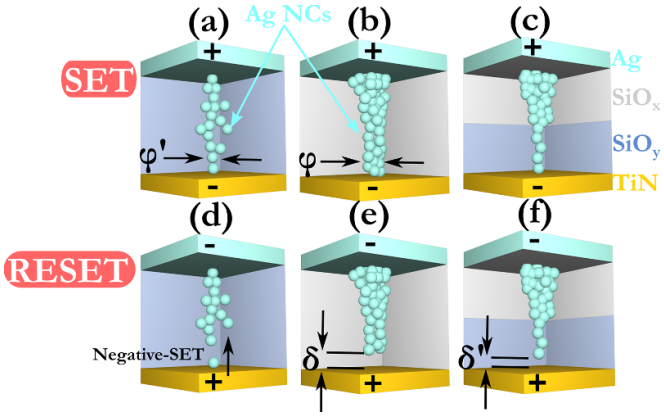

Figure 7. Schematic depiction of the CF growth and dissolution procedure for (a), (d) sample A, (b), (e) sample B and (c), (f) sample C, during SET/RESET transitions. The symbols φ and δ stand for the effective diameter of the CF and the gap size, respectively.

we report that the impact of just 4% doping with oxygen during the growth of the film can yield in enhanced and reconfigurable resistive switching as well as neuromorphic properties. Experiments with 0% doping were also carried out in order to assess the minimum oxygen doping required in order to achieve robust resistive switching and neuromorphic properties. However, the results divulged (not shown here) an unstable memory performance which made the implementation of various synaptic properties difficult. Bearing in mind that only one CF suffices in order to alter the device's resistance, controlling its properties is quite crucial towards implementing a wide range of neuromorphic properties. As a result, we can argue that the STP can be emulated by relatively small CFs (effective diameter <1 nm) that will self-dissolve after the stimulus stops to apply and the LTP by larger CFs (effective diameter 5–6 nm) that will retain their initial configuration for a long period of time, even when the external stimulus has been removed. The above-mentioned estimations of the CF's diameter stem from the application of a previously reported numerical model (not shown here) [11] in order to interpret the experimental results. Figure 7 illustrates a schematic representation of the principal switching mechanism for all samples. In all cases, the switching effect begins with the migration of cations from the electrochemically active TE, through drift and diffusion mechanisms. Since the diffusion of metals within SiO_2 is anticipated to be interstitial in principle (the vacancy diffusion mechanism is relatively slower), the density of oxygen ions will strongly affect the activation energy required for ions to migrate from an interstitial site to another one [38]. In the literature, there are many reports regarding the impact of oxygen flow rate during the fabrication process of radiofrequency (RF) sputtered SiO_2 thin films [39–41]. The common denominator of these works is that an elevated oxygen concentration leads to an increased number of O_2 interstitials, as we have ascertained above from the XPS results. This effect implies that the diffusing ions need to overcome a higher potential barrier, which is formed as a result of the induced geometric reordering of the neighboring atoms. Thus, it will be more difficult for the silver cations to find a

potential percolating path in order to reach the inactive BE and be reduced. The activation energy required in order for a migrating atom to move through the host material can be expressed as follows [42]:

$$E_a = 4\pi G r_d (r - r_d)^2 \quad (2)$$

where G is the shear modulus, r is the radius of the migrating atom and r_d is the available radius window that the migrating atom must pass through. A higher diffusing barrier will lead thus to the formation of smaller CF for sample A, in terms of effective diameter distribution, in contrast with sample B ($\varphi' < \varphi$—figures 7(a) and (b)), which in conjunction with the local Joule heating effects will lead to a permanent volatile behavior. The coexistence of threshold and bipolar switching for sample B can be interpreted by size-dependent melting process of the Ag nanoclusters [43], which are formed due to material precipitation from the enhanced solid-solubility of Ag [11].

On the other hand, for the bilayer material configuration (sample C) only the bipolar switching mode is observed, since the oxygen poor layer (SiO_x) serves practically the role of a virtual anode which supplies the oxygen rich layer (SiO_y) with ions [44]. Consequently, the CF is less susceptible to thermal instabilities, due to its spatial confinement effect, and thus cannot be self-ruptured (figure 7(c)) [45]. The existence of truncated-cone CF for samples B and C has been adopted in order to account for the self-rectification properties of these devices. This selection is also in line with concrete experimental and theoretical evidences for SiO_2-based CBRAM [46, 47]. Moreover, a smaller gap for the RESET transition is anticipated for sample C in respect to sample B (($\delta' < \delta$—figures 7(e) and (f))) in order to account for the higher current values of the HRS. In addition, the broken region of the CF for sample A is expected to take place not at CF/BE interface but deeper within the CF, in order to account for the bidirectional threshold switching effect (figure 7(d)). Although the origins of this behavior are not clear, the dependence of the CF's thermal conductivity from its diameter affects decisively the total temperature distribution. From the above analysis, it is apparent that the reconfigurable neuron and synaptic properties of our devices are closely correlated with the respective CF growth mode. For small external triggering conditions ($\sim$100 mV) we achieve artificial neuron properties only for samples A and B, which exhibit the threshold switching effect and the CF exhibits an unstable behavior. The same pattern applies also for the STP artificial synaptic properties under the application of larger pulses ($\sim$300 mV), whereas the emergence of the bipolar switching behavior is connected with the manifestation of LTP effects.

5. Conclusion

In conclusion, we demonstrate the existence of various resistive switching modes and their impact on the manifestation of diverse neuromorphic properties in SiO_2-based memristors. The oxygen concentration within the dielectric matrix provides unique opportunities towards controlling the growth mode and the properties of the CF. A relatively fragile CF can be leveraged in order to demonstrate artificial neuron and STP properties since it is ascribed with the volatile nature of the switching effect. On the contrary, a more robust CF is used towards the implementation of LTP synaptic effects due the emergence of the more stable bipolar switching mode. These results provide an effective method towards the emulation of artificial neuron and synaptic properties from the same material configuration and create new approaches towards the fabrication of fully memristive neural networks.

6. Experimental section

6.1. Device fabrication

The thin films were deposited on oxidized silicon substrates by RF magnetron sputtering technique. All depositions were carried out at room temperature. The main chamber that was used for the depositions possessed a base pressure of about 2×10^{-6} mbar prior the plasma ignition though Ar gas injection. During the depositions the pressure was about 4×10^{-3} mbar. A high purity ceramic target (SiO_2 target—99.99%) was employed during the deposition of the 20 nm thin film of SiO_2. The flow of Ar during the deposition was kept constant during the deposition at 20 sccm while for O_2 two different flows were used (1 sccm and 5 sccm). For the fabrication of the bilayer configuration the oxygen flow was changed from 5 sccm to 1 sccm when the first 10 nm were deposited. The TiN (BE) and Ag (TE) were accordingly deposited by the respective TiN and Ag sputtering targets with a total thickness of 40 nm. A total power of 140 W and 200 W was delivered onto the ceramic targets (SiO_2, TiN) and metallic targets (Ag), respectively. The fabricated devices were typical metal-insulator-metal capacitors with square electrodes of 100 μm lateral dimension.

6.2. Electrical performance characterization

The DC *I*–*V* characteristics of the devices were performed with the Keithley 4200 semiconductor parameter analyzer (4200-SCS) at SUSS MicroTec probe station. The pulsed *I*–*V* measurements were conducted by employing the Keithley 4225-PMU (pulse measurement unit). Moreover, *C*–*V* measurements were carried out with the 4284A Precision LCR Meter. In addition, temperature measurements were performed at Janis Ltd Cryostat (-193 °C–200 °C) under vacuum conditions ($\sim 10^{-2}$ mbar).

6.3. Structural characterization

The photoemission experiments were carried out in an ultra-high vacuum system (UHV—10^{-10} mbar) equipped with a dual anode x-ray gun and Phoibos 100 1D-DLD electron analyser. Unmonochromatized MgKα line at 1253.6 eV and an analyzer pass energy of 10 eV, giving a full width at half maximum of 0.85 eV for the Ag3d5/2 peak, were used in all XPS measurements. Spectra were accumulated and fitted

using commercial software (SpecsLab Prodigy; Specs GmbH, Berlin). The XPS core level spectra were analyzed using a fitting routine, which can decompose each spectrum into individual mixed Gaussian–Lorentzian peaks after a Shirley background subtraction. Wide Scans were recorded for all samples, while the core level peaks that were recorded in detail and presented here were: O1s, Si2p and Ar2p. Errors in our quantitative data are found in the range of ∼10% (peak areas), while the accuracy for BEs assignments is ∼0.1 eV. The Veeco dektak 150 surface profiler as well as the M2000F by Woollam Co spectroscopic ellipsometer equipments were used in order to measure the thickness of each film.

Data availability statement

The data that support the findings of this study are available upon reasonable request from the authors.

Acknowledgments

This research is funded in the context of the project 'Electronic switching resistance memories made from SiO_x and metallic nanoparticles for neuromorphic applications' (MIS 5049432) under the call for proposals 'Researchers' support with an emphasis on young researchers—2nd Cycle'. The project is co-financed by Greece and the European Union (European Social Fund—ESF) by the Operational Programme Human Resources Development, Education and Lifelong Learning 2014-2020. We are also grateful to Mr D Sakellaropoulos and Mr S Kitsios for technical assistance during sample preparation as well as to Dr L Syggelou for carrying out the XPS measurements at the Institute of Chemical Engineering Sciences (FORTH/ICEHT).

ORCID iDs

Panagiotis Bousoulas https://orcid.org/0000-0002-5395-0777
Dimitris Tsoukalas https://orcid.org/0000-0001-5189-3396

References

[1] Sebastian A, Gallo M L, Aljameh R K and Eleftheriou E 2020 Memory devices and applications for in-memory computing *Nat. Nanotechnol.* **15** 529–44
[2] Ielmini D and Ambrogio S 2020 Emerging neuromorphic devices *Nanotechnology* **31** 092001
[3] Li C *et al* 2018 Analogue signal and image processing with large memristor crossbars *Nat. Electron.* **1** 52
[4] Jang B C, Kim S, Yang S Y, Park J, Cha J H, Oh J, Choi J, Im S G, Dravid V P and Choi S Y 2019 Polymer analog memristive synapse with atomic-scale conductive filament for flexible neuromorphic computing system *Nano Lett.* **19** 839
[5] Wang P, Khan A I and Yu S 2020 Cryogenic behavior of NbO_2 based threshold switching devices as oscillation neurons *Appl. Phys. Lett.* **116** 162108
[6] Wang Z *et al* 2018 Fully memristive neural networks for pattern classification with unsupervised learning *Nat. Electron.* **1** 137
[7] Pantazi A, Woźniak S, Tuma T and Eleftheriou E 2016 All-memristive neuromorphic computing with level-tuned neurons *Nanotechnology* **27** 355205
[8] Li H Y *et al* 2020 Controlled memory and threshold switching behaviors in a heterogeneous memristor for neuromorphic computing *Adv. Electron. Mater.* **6** 2000309
[9] Kurenkov A, DuttaGupta S, Zhang C, Fukami S, Horio Y and Ohno Y 2019 Artificial neuron and synapse realized in an antiferromagnet/ferromagnet heterostructure using dynamics of spin–orbit torque switching *Adv. Mater.* **31** 1900636
[10] Abbas H, Abbas Y, Hassan G, Sokolov A S, Jeon Y R, Ku B, Kangd C J and Choi C 2020 The coexistence of threshold and memory switching characteristics of ALD HfO_2 memristor synaptic arrays for energy-efficient neuromorphic computing *Nanoscale* **12** 14120
[11] Bousoulas P, Sakellaropoulos D, Papakonstantinopoulos C, Kitsios S, Arvanitis C, Bagakis E and Tsoukalas D 2020 Investigating the origins of ultra-short relaxation times of silver filaments in forming-free SiO_2-based conductive bridge memristors *Nanotechnology* **31** 454002
[12] Jensen D S, Kanyal S S, Madaan N, Vail M A, Dadson A E, Engelhard M H and Linford M R 2013 Silicon (100)/SiO_2 by XPS *Surf. Sci. Spectra* **20** 36
[13] Swart H C, Van Hattum E D, Arnoldbik W M and Habraken F H P M 2004 Comparison of SiO_x structure in RF sputtered samples *Phys. Status Solidi* c **1** 2286–91
[14] Tomozeiu N 2006 SiO_x thin films deposited by r.f. magnetron reactive sputtering: structural properties designed by deposition conditions *J. Optoelectron. Adv. Mater.* **8** 769–75
[15] Van Hattum E D, Palmero A, Arnoldbik W M and Habraken F H P M 2004 Experimental characterization of the deposition of silicon suboxide films in a radiofrequency magnetron reactive sputtering system *Surf. Coat. Technol.* **188–189** 399–403
[16] Tomozeiu N, Van Hapert J J, Van Faasen E E, Arnoldbik W, Vredenberg A M and Habraken F H P M 2002 Structural properties of a-SiO_x layers deposited by reactive sputtering technique *J. Optoelectron. Adv. Mater.* **4** 513–21
[17] Himpsel F J, McFeely F R, Ibrahimi A T, Yarmoff J A and Hollinger G 1988 Microscopic structure of the SiO_2/Si interface *Phys. Rev.* B **38** 6084
[18] Van Hattum E D, Palmero A, Arnoldbik W, Rudolph H and Habraken F H P M 2007 Distinct processes in radio-frequency reactive magnetron plasma sputter deposition of silicon suboxide films *J. Appl. Phys.* **102** 124505
[19] Arnoldbik W, Van Emmichoven P A Z and Habraken F H P M 2005 Electronic sputtering of silicon suboxide films by swift heavy ions *Phys. Rev. Lett.* **94** 245504
[20] Zhang Y *et al* 2018 Highly compact artificial memristive neuron with low energy consumption *Small* **14** 1802188
[21] Wang W, Wang M, Ambrosi E, Bricalli A, Laudato M, Sun Z, Chen X and Ielmini D 2019 Surface diffusion-limited lifetime of silver and copper nanofilaments in resistive switching devices *Nat. Commun.* **10** 81
[22] Lim H, Kornijcuk V, Seok J Y, Kim S K, Kim I, Hwang C S and Jeong D S 2015 Reliability of neuronal information conveyed by unreliable neuristor based leaky integrate-and-fire neurons: a model study *Sci. Rep.* **5** 9776
[23] Yang R *et al* 2018 Synaptic suppression triplet-STDP learning rule realized in second-order memristors *Adv. Funct. Mater.* **28** 1704455
[24] Wang Z *et al* 2018 Capacitive neural network with neuro-transistors *Nat. Commun.* **9** 3208

[25] Stoliar P, Tranchant J, Corraze B, Janod E, Besland M P, Tesler F, Rozenberg M and Cario L 2017 A leaky-integrate-and-fire neuron analog realized with a Mott insulator *Adv. Funct. Mater.* **27** 1604740
[26] Mehonic A and Kenyon A J 2016 Emulating the electrical activity of the neuron using a silicon oxide RRAM cell *Front. Neurosci.* **10** 57
[27] Zhang X *et al* 2018 An artificial neuron based on a threshold switching memristor *IEEE Electron Device Lett.* **39**
[28] Zhao X *et al* 2018 Breaking the current-retention dilemma in cation-based resistive switching devices utilizing graphene with controlled defects *Adv. Mater.* **30** 1705193
[29] Lee D *et al* 2019 Various threshold switching devices for integrate and fire neuron applications *Adv. Electron. Mater.* **5** 1800866
[30] Lübben M, Cüppers F, Mohr J, Von Witzleben M, Breuer U, Waser R, Neumann C and Valov I 2020 Design of defect-chemical properties and device performance in memristive systems *Sci. Adv.* **6** eaaz9079
[31] Bousoulas P, Karageorgiou I, Aslanidis V, Giannakopoulos K and Tsoukalas D 2017 Tuning resistive, capacitive, and synaptic properties of forming free TiO_{2-x}-based RRAM devices by embedded Pt and Ta nanocrystals *Phys. Status Solidi* a **215** 1700440
[32] Lu Y F, Li Y, Li H, Wan T Q, Huang X, He Y H and Miao X 2020 Low-power artificial neurons based on Ag/TiN/$HfAlO_x$/Pt threshold switching memristor for neuromorphic computing *IEEE Electron Device Lett.* **41** 8
[33] Takeuchi T, Duszkiewicz A J and Morris R G M 2014 The synaptic plasticity and memory hypothesis: encoding, storage and persistence *Phil. Trans. R. Soc.* B **369** 20130288
[34] Wang Z *et al* 2016 Memristors with diffusive dynamics as synaptic emulators for neuromorphic computing *Nat. Mat.* **16** 101
[35] Shiffrin R M and Atkinson R C 1969 Storage and retrieval processes in long-term memory *Psychol. Rev.* **76** 179
[36] Ohno T, Hasegawa T, Tsuruoka T, Terabe K, Gimzewski J K and Aono M 2011 Short-term plasticity and long-term potentiation mimicked in single inorganic synapses *Nat. Mater.* **10** 591
[37] Zhang Y, Zhong S, Song L, Ji X and Zhao R 2018 Emulating dynamic synaptic plasticity over broad timescales with memristive device *Appl. Phys. Lett.* **113** 203102
[38] Shewmon P G 1963 *Diffusion in Solids* (New York: McGraw-Hill)
[39] Afsharipour E, Park B and Shafai C 2017 Determination of reactive RF-sputtering parameters for fabrication of SiO_x films with specified refractive index, for highly reflective SiO_x distributed Bragg reflector *IEEE Photon. J.* **9** 2700116
[40] Kajihara K, Kamioka H, Hirano M, Miura T, Skuja L and Hosono H 2016 Interstitial oxygen molecules in amorphous SiO_2. II. The influence of common dopants (SiOH, SiF, and SiCl groups) and fictive temperature on the decay of singlet photoluminescence *J. Appl. Phys.* **98** 013528
[41] Holmen G and Jacobsson H 1990 The influence of oxygen on SiO_2 sputtering *J. Appl. Phys.* **68** 2962
[42] McBrayer J D, Swanson R M and Sigmon T W 1986 Diffusion of metals in silicon dioxide *J. Electrochem. Soc.* **133** 1242
[43] Magdassi S, Grouchko M, Berezin O and Kamyshny A 2010 Triggering the sintering of silver nanoparticles at room temperature *ACS Nano* **4** 1943
[44] Bousoulas P, Asenov P, Karageorgiou I, Sakellaropoulos D, Stathopoulos S and Tsoukalas D 2016 Engineering amorphous-crystalline interfaces in TiO_{2-x}/TiO_{2-y}-based bilayer structures for enhanced resistive switching and synaptic properties *J. Appl. Phys.* **120** 154501
[45] Sun Y M *et al* 2019 Modulating metallic conductive filaments via bilayer oxides in resistive switching memory *Appl. Phys. Lett.* **114** 193502
[46] Sun H, Liu Q, Li C, Long S, Lv H, Bi C, Huo Z, Li L and Liu M 2014 Direct observation of conversion between threshold switching and memory switching induced by conductive filament morphology *Adv. Funct. Mater.* **24** 5679–86
[47] Yang Y, Gao P, Gaba S, Chang T, Pan X and Lu W 2012 Observation of conducting filament growth in nanoscale resistive memories *Nat. Commun.* **3** 732